Titre: Title:	Back to basics – NO concentration measurements in atmospheric lean-to-rich, low-temperature, premixed hydrogen–air flames diluted with argon
Auteurs: Authors:	Antoine Durocher, Marie Meulemans, Philippe Versailles, Gilles Bourque, & Jeffrey M. Bergthorson
Date:	2021
Type:	Article de revue / Article
Référence: Citation:	Durocher, A., Meulemans, M., Versailles, P., Bourque, G., & Bergthorson, J. M. (2021). Back to basics – NO concentration measurements in atmospheric lean-to-rich, low-temperature, premixed hydrogen–air flames diluted with argon. Proceedings of the Combustion Institute, 38(2), 2093-2100. https://doi.org/10.1016/j.proci.2020.06.124

Titre de la revue: Journal Title:	Proceedings of the Combustion Institute (vol. 38, no. 2)
Maison d'édition: Publisher:	Elsevier
URL officiel: Official URL:	https://doi.org/10.1016/j.proci.2020.06.124
Mention légale: Legal notice:	

Available online at www.sciencedirect.com

ScienceDirect

Proceedings of the Combustion Institute 38 (2021) 2093–2100

Proceedings of the Combustion Institute

www.elsevier.com/locate/proci

Back to basics – NO concentration measurements in atmospheric lean-to-rich, low-temperature, premixed hydrogen–air flames diluted with argon

Antoine Durocher [a,*], Marie Meulemans [a], Philippe Versailles [b], Gilles Bourque [a,b], Jeffrey M. Bergthorson [a]

[a] *McGill University, 845 Sherbrooke St W, Montreal, QC H3A 0G4, Canada*
[b] *Siemens Canada Limited, 9505 Côte-de-Liesse, Dorval, QC H9P 1A5, Canada*

Received 7 November 2019; accepted 28 June 2020
Available online 24 August 2020

Abstract

Ideally, nitric oxide (NO) production pathways would be measured individually to understand the formation mechanisms at a fundamental level. Unfortunately, the four production routes in hydrocarbon combustion cannot be fully decoupled. Hydrogen combustion at low flame temperatures eliminates prompt-NO and mitigates thermal production, such that only the N_2O and NNH pathways remain as significant production routes. The H_2/O_2 system, whose base chemistry has been studied in great detail, offers an excellent platform to validate nitrogen chemistry by limiting the possibility of error propagation during model calibration. The current work presents measurements of velocity, temperature, and NO concentration in premixed, jet-wall stagnation, hydrogen–air flames at atmospheric pressure, diluted with argon to maintain adiabatic flame temperatures below 1800 K. Measurements of reference flame speeds, $S_{u,ref}$, obtained with particle tracking velocimetry, highlight the modeling differences in H_2/O_2 chemistry from a selection of thermochemical mechanisms, especially in lean flames affected by preferential diffusion. Laser induced fluorescence measurements in lean-to-rich flames ($\phi = 0.7$–1.5) yield concentrations of NO from 2 to 0.5 ppm, respectively. Simulated NO profiles cover one order of magnitude in predicted signal intensity. Fortunately, recent mechanisms with accurate descriptions of the N_2O and NNH pathways predict NO concentrations within experimental uncertainties for multiple operating conditions.

Keywords: H_2 premixed flames; NO-Laser induced fluorescence; Particle tracking velocimetry; Emission modeling

1. Introduction

Engine manufacturers must actively develop low-emissions architectures to mitigate the negative effects of nitrogen oxides (NO_x) on human health and the environment. In an effort to

* Corresponding author.
E-mail address: antoine.durocher@mail.mcgill.ca (A. Durocher).

https://doi.org/10.1016/j.proci.2020.06.124

minimize the formation of nitric oxide through the dominant thermal (Zel'dovich) pathway, lean, premixed configurations have emerged and are able to achieve sub–10 ppm emission levels [1]. In these conditions, the formation via the prompt, N_2O, and NNH routes is expected to contribute significantly to emissions [2]. The fundamental understanding of these chemical pathways is not as well developed as for thermal NO production and sensitizing experiments to single out each formation route is difficult, if not impossible, in hydrocarbon fuels.

As a carbon-free fuel, hydrogen has the advantage of having only three NO production channels: thermal, N_2O, and NNH [3]. By controlling flame temperatures with dilution, it is also possible to mitigate the formation through the thermal pathway, leaving only two active formation routes. Few experimental campaigns, however, focused on pure hydrogen flames. Quantitative NO measurements were performed in low-pressure McKenna burners with H_2/N_2O [4] and to provide evidence of the NNH production route [5], and in counterflow flames with various diluents [6]. In summary, only a handful of data sets with hydrogen has been obtained to provide fundamental understanding of the NO_x formation mechanisms in flames of the simplest fuel [3,7].

A detailed and precise understanding of the H_2/O_2 system is essential in combustion science. This rather "simple" chemistry has received repeated interest from the community to capture specific reaction rates with increasing accuracy and to reduce uncertainty [8]. It provides an ideal platform to validate nitrogen chemistry with minimal error propagation from the core chemistry to quantify prediction uncertainty [9] and constrain mechanisms to finally develop predictive models [10].

The current paper provides a new independent set of experimental measurements for velocity, temperature, and NO concentration in premixed, jet-wall stagnation, hydrogen–air flames from lean to rich equivalence ratios. The mixtures are diluted with argon to maintain adiabatic flame temperatures below 1800 K. The accuracy of thermochemical mechanisms to predict flame reactivity and NO formation is assessed for various models and reaction pathway analyses (RPA) estimate the relative contribution from the NNH and N_2O routes. Detailed boundary conditions are provided to allow for accurate flame simulations, such that the data can be used as validation targets in model development.

2. Jet-wall stagnation flame experimental facility

The experiments are performed in a high-pressure laminar flame facility [2,11] under atmospheric pressure. A jet-wall stagnation burner is used to obtain compact, stable, and lifted flames that are minimally affected by the boundary conditions, and allow for non-intrusive laser diagnostics for measurements of reactivity, temperature, and concentrations.

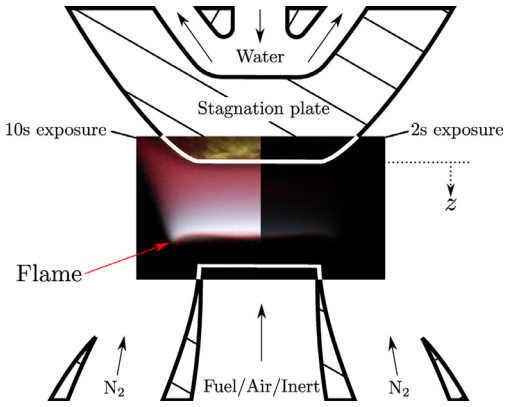

Fig. 1. Jet-wall stagnation burner with a hydrogen flame.

The burner, shown in Fig. 1 with a hydrogen flame captured with varying exposure time, is centered in an enclosure equipped with two pairs of sapphire glass windows to allow laser-based diagnostics. The diluted combustible mixture exits the inner nozzle with a throat diameter of 10.2 mm and impinges on a water-cooled stagnation surface ~9 mm downstream of the nozzle. The flame stabilizes at the location where the flow velocity matches its stretched flame speed. The position is monitored throughout the experiment with ultraviolet chemiluminescence to ensure flame stability. The temperatures of the inlet mixture and the stagnation surface are monitored with K-type thermocouples, and the plate temperature is maintained below ~425 K to avoid surface reactions. Thermal mass flow controllers, calibrated with a dry-piston calibrator, control the fuel, air, argon, and nitrogen flows.

Experimental boundary conditions are reported in the Supplemental Material for all mixtures studied. Velocity boundary conditions are extracted from a least-squares parabolic fit in the cold flow region upstream of the flame measured with particle tracking velocimetry described in Section 2.1. Simulations are performed with Cantera 2.4 [12] using the multi-component formulation for species transport, as well as radiative heat losses. The Soret effect, necessary in lean hydrogen flames [13], is included. Solutions are converged to absolute and relative tolerances of 10^{-9} and 10^{-5}, respectively. The computational grid is refined to obtain gradient and curvature parameters of 0.03, resulting in solutions with ~450 grid points.

2.1. Particle tracking velocimetry

Two-dimensional (2D) Particle Tracking Velocimetry (PTV) is used to measure axial and

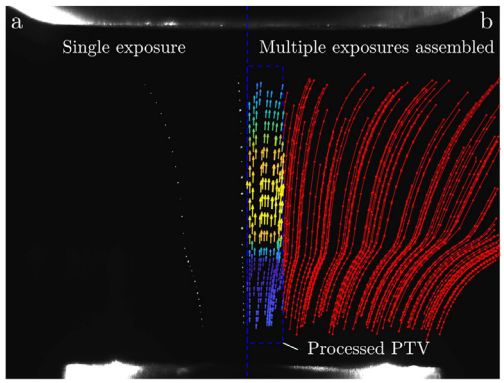

Fig. 2. Particle tracking velocimetry for (a) a single exposure and (b) the assembled 2D field. Streak and velocity vector densities are reduced for readability.

radial velocity fields. Details on the experimental setup can be found in [2,11]. The beam produced by a diode pumped, dual cavity, high-repetition rate Nd:YLF laser is horizontally compressed by borosilicate glass lenses. Refractory 1 μm alumina particles are seeded in the combustible mixture and illuminated by the thin ($\sim$1 mm) laser sheet centered above the nozzle centerline axis. The laser frequency is adjusted for each experiment (6–12 kHz) to maximize resolution in the cold flow region. The scattered light is focused on a 14-bit monochrome CCD camera. Several irradiation events are acquired on single images resulting in streaks of dots analogous to streamlines (Fig. 2a). A second-order accurate, central finite difference scheme calculates the particle velocity, u_p, from the particle location spatially calibrated with a dotted target (Thorlabs R2L2S3P3) [11]. Hundreds of streaks are accumulated to obtain 2D velocity fields (Fig. 2b). One-dimensional (1D) velocity profiles are then extracted from data in the vicinity of the centerline axis. Direct comparisons between measurements and simulations are made possible through simulated PTV [14]. Newton's second law, including particle lag due to thermophoretic forces and inertia, is applied to a virtual particle seeded in the flow to recover its trajectory. The expected PTV velocity is then calculated with the same second-order scheme used in the experimental data processing.

2.2. Planar NO laser-induced fluorescence

Two-dimensional, planar laser-induced fluorescence (LIF) is used to measure NO concentration with the setup presented in detail in [2,15]. The beam produced by a Nd:YAG-pumped wavelength tunable dye laser filled with a solution of Coumarin 450 dye is passed through a frequency doubling crystal before fused-silica lenses collimated it into a $\sim$9 mm tall, $\sim$1 mm wide, sheet aligned above the nozzle centerline axis. The online laser wavelength, λ_{on}, is adjusted to $\sim$226.03 nm in the A–X (0,0) electronic system of NO which contains the $P_1(23.5)$, $Q_1 + P_{21}(14.5)$, and $Q_2 + R_{12}(20.5)$ transitions. Offline signals are obtained at a theoretical absorption minimum located at $\sim$226.05 nm to subtract interfering O_2-LIF signals. The fluorescence signal is collected by an ultraviolet, achromatic lens equipped with a long-pass filter. Images are captured with a monochromatic, 12-bit, intensified CCD camera illuminated during a 50 ns gate time to minimize flame chemiluminescence. Signal-to-noise is increased by binning 4 (vertically) and 8 (horizontally) pixels to achieve a resolution of 0.105 mm/pixel axially, and accumulating 20 exposures on the ICCD before readout to allow measurements of sub–ppm concentration levels.

Experimental online, offline, and background signals, S_{on}, S_{off}, and S_{bckg}, respectively, are obtained by averaging 500 images for the LIF signals and 100 for the background resulting in 10,000 laser irradiation events and 2,000 background exposures. The NO signal is obtained using Eq. (1) by subtracting the measured signals normalized by the laser energy, E_L, obtained by integrating the laser pulse power profile measured by a photodiode with an oscilloscope. Signals are also corrected for spatial variation in the laser sheet intensity using an averaged LIF image collected in a cold flow with a constant amount of NO seeded in an inert mixture of Ar and N_2. One-dimensional profiles are extracted by averaging 20 pixels radially ($\sim$ 4.2 mm) to increase signal-to-noise ratio at each axial location.

$$S_{NO} = (S_{on} - S_{bckg}) - (S_{off} - S_{bckg}) \times E_{L,on}/E_{L,off} \tag{1}$$

For weak laser irradiation, the resulting NO–LIF signal in the linear regime is described by

$$\frac{S_{NO}}{E_L} = C_{opt} \cdot f_{LIF}(f_B, \lambda, \Delta\nu_L, \Gamma, A_{21}, B_{12}, Q_{21}) \times n^{\circ}_{NO}, \tag{2}$$

where the calibration constant C_{opt} accounts for the transmissivity and the characteristics of the optical detection system, f_{LIF} is the number of emitted photons per number of NO molecules and laser energy, and $n^{\circ}_{NO}(T, P, X_{NO})$ is the number density of NO molecules. The LIF signal described by absorption and emission processes is a function of the Boltzmann fraction $f_B(T)$ of NO molecules excited by the laser, the excitation wavelength λ, the spectral width of the laser $\Delta\nu_L$, the dimensionless overlap Γ, the Einstein constant of absorption A_{12}, the rate constant of emission B_{21}, and the rate of collisional quenching Q_{21}. Limitations in the available species (N_2, O_2, H_2O, CO_2, CO, CH_4, and Ar) prevent the use of readily available detailed LIF models used in [2,16] for hydrogen–air flames as non-negligible concentrations of H

and OH species affect the effective cross-section for collisional quenching [17]. The two-level LIF model of Eq. (3) [16] is implemented to generate computational signals where c is the speed of light and Q_{21} is evaluated from Tamura et al. [18].

$$\frac{S_{NO}}{C_{opt}E_L} = \frac{B_{12}}{c}\frac{f_B\Gamma}{\Delta\nu_L}\frac{A_{21}}{A_{21}+Q_{21}}n^{\circ}_{NO} \quad (3)$$

Calibration of the optical constant, C_{opt}, detailed in Supplemental Material, is performed similarly to [16,19] with a known amount of seeded NO in the reactant stream (5, 10, and 15 ppm) in the leanest flame ($\phi = 0.7$). Under the assumption that, in this low-temperature lean condition, there is no reburn or recombination of NO species, the subtraction of the experimental unseeded fluorescence signal from the seeded one yields a net intensity that is a function of the known, non-reacting, NO seeding. With known boundary conditions, this methodology is reproduced numerically using Cantera and the two-level LIF model to obtain a net numerical profile minimally affected by the choice of nitrogen chemistry, provided that the base chemistry adequately captures the reactivity and thermochemistry. The calibration constant, C_{opt}, is then calculated using a least-square minimization between the net experimental and numerical profiles in the entire post-flame region, from the flame front until the thermal boundary layer near the water-cooled stagnation surface. The averaged C_{opt} obtained from the calibration of the three seeded mixtures is used to quantify the measurements.

Direct comparison of measured and simulated 1D profiles is performed using the methodology suggested by Connelly et al. [20] to minimize the uncertainty in experimental data introduced by assumptions in temperature and species concentration fields. Numerical LIF signals generated with complete laminar stagnation flame solutions are compared directly with relatively raw experimental measurements with an uncertainty of $\sim$20% that accounts for spatial calibration, fluctuations in signal intensity and laser energy, and C_{opt}.

2.3. Multi-line NO-LIF thermometry

The A–X(0,0) electronic system is used to maximize temperature sensitivity while minimizing interfering signals. The scan ranges from 225.13 nm to 225.19 nm similarly to [16] with a spectral resolution of 0.61 pm and covers 7 rotational transitions blended into 4 temperature-dependent features. Signals are averaged for 50 images at each wavelength, and corrected for laser pulse energy. Approximately 500 ppm of NO is seeded in the flames to monitor temperature through the entire domain. Unseeded scans are subtracted to remove background noise and interfering signals.

The 1D signal is obtained by averaging a few pixels across the centerline at each axial and spectral location. Experimental excitation spectra for NO emission intensity are assembled for the range of wavelengths studied and compared to numerical spectra obtained with LIFBase [21]. A non-linear least-square fitting procedure minimizes the difference between the experimental and numerical profiles to determine the gas temperature [15]. Good agreement between fitted and experimental excitation profiles was shown with an uncertainty in temperature measurements of approximately $\pm$5% [22].

3. Results and discussion

A summary of the experimental results is shown in Fig. 3 for lean ($\phi = 0.7$), stoichiometric ($\phi = 1.0$), and rich ($\phi = 1.5$) cases with velocity, temperature, and NO-LIF profiles presented from top to bottom. Direct comparisons with five thermochemical mechanisms assess their capability to accurately capture the reactivity and NO formation. Mechanisms including hydrocarbon chemistry have been reduced to contain species composed only of H/N/O atoms and inert gases. The mechanisms considered are: (1) the GRI mechanism 3.0 (GRI) [23]; (2) the San Diego 2016 (SD) mechanism [24] including the updated 2018 nitrogen chemistry; (3) the Chemical Reaction Engineering and Chemical Kinetics laboratory (CRECK) model v1412 [25]; (4) a recently assembled version of the National University of Ireland Galway (NUIG) mechanism [26] for high-temperature chemistry with the nitrogen chemistry of Glarborg et al. [3]; (5) the most recent hydrogen mechanism by Konnov (KON) [27] which incorporates chemically termolecular reactions and updates in transport properties, but does not include nitrogen chemistry. To isolate the effects of the nitrogen chemistry, Fig. 3(j–l) presents simulation results for mechanisms assembled from the base chemistry of the NUIG mechanism and the nitrogen chemistry of GRI, SD, and CRECK.

Particle velocity profiles (Fig. 3a–c) capture the expected behavior with the flow decelerating from the inlet before rapidly accelerating through the flame front and decelerating as it impinges on the stagnation surface located at $z = 0$ mm. The stability of the hydrogen flames is confirmed by the PTV measurements, as shown by the sharp flame front. Significant discrepancy is observed between mechanisms, especially in lean conditions, where the Soret effect greatly affects species transport. Predictions of the reference flame speed, $S_{u,ref}$, defined as the velocity minimum upstream of the flame, vary by as much as 20% between models. For all flames, the NUIG mechanism agrees well with measurements, slightly over-predicting the velocity of richer flames. The remaining mechanisms

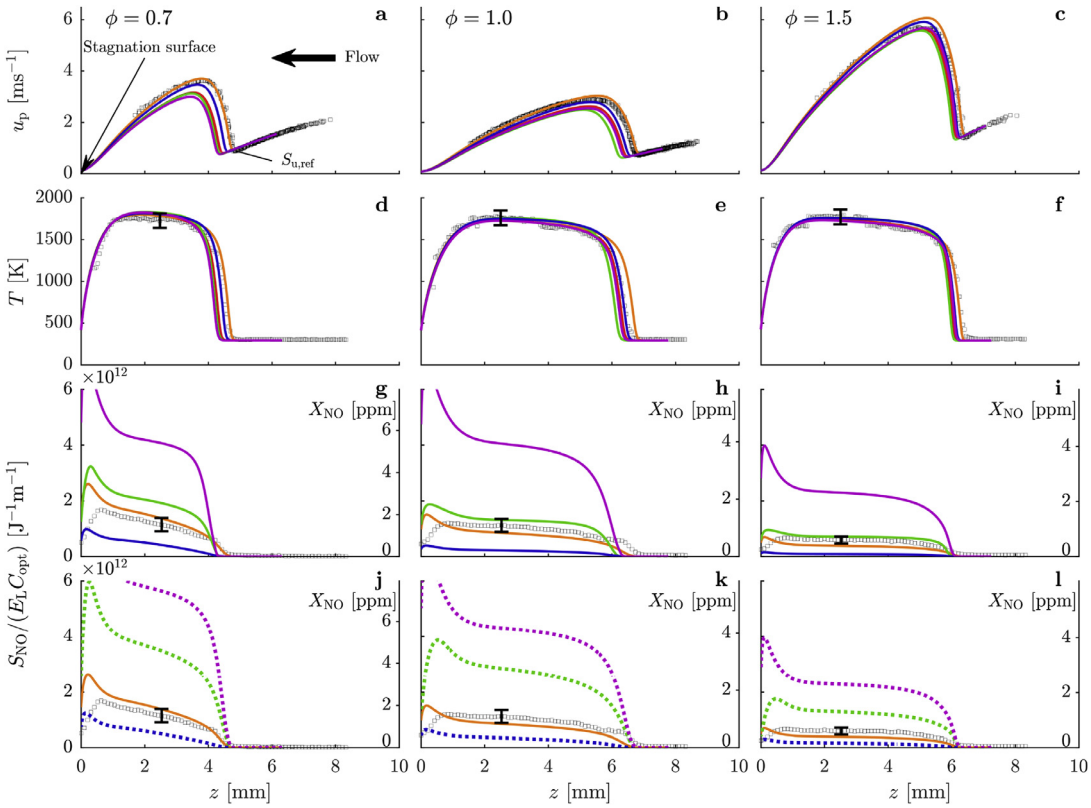

Fig. 3. Particle velocity, temperature, and NO-LIF signal profiles for lean ($\phi = 0.7$ – left), stoichiometric ($\phi = 1.0$ – center), and rich ($\phi = 1.5$ – right) cases. Thermochemical mechanisms are: GRI (magenta), SD (blue), CRECK (green), NUIG (orange), and KON (red). Predictions for nominal mechanisms are given by solid lines. Dashed lines denote results obtained for mechanisms assembled from the NUIG base chemistry with the nitrogen chemistry from the remaining mechanisms presented here.

systematically under-predict the reactivity of the mixtures.

Temperature profiles (Fig. 3d–f) capture the sharp increase at the flame front and the cooling near the stagnation surface. Simulated profiles show good agreement amongst them and with experimental data, indicating an adequate definition of the thermodynamic properties to capture flame temperature within experimental uncertainties. Measurements in lean-to-rich flames confirm that flame temperatures are slightly below the expected adiabatic temperature of 1800 K, ranging from ~1725 K–1785 K, which is expected to minimize the formation of NO through the thermal pathway.

NO-LIF intensity profiles normalized by laser energy and C_{opt} (Fig. 3g–l) exhibit a sharp increase in concentration at the flame front with a relatively small formation in the post flame region for leaner conditions, as expected from the flame temperatures. With no prompt-NO produced with hydrogen, the formation observed in the flame front is, therefore, a result of the NNH and N_2O pathways. The sharp peak in signal intensity near the stagnation surface is attributed to the increase in number density near the cooled plate before nitric oxide is consumed. Estimates in ppm, valid upstream of the stagnation-surface thermal boundary layer, are provided to facilitate comparison. The calibration of C_{opt} is performed with the NUIG mechanism that exhibits the best overall agreement with velocity and temperature measurements. A validation of the methodology is performed with GRI to ensure that the calculation of C_{opt} is robust to the choice of mechanism. Calculated values with each model are within 1%, well inside the experimental uncertainty.

Significant discrepancies between nominal model predictions and measurements are observed in Fig. 3(g–i) for the GRI and SD mechanisms which greatly over- and under-estimate the NO formation in the flame front leading to predictions spanning one order of magnitude. Although relatively good agreement can be observed in specific cases for these mechanisms with hydrocarbon fuels, these discrepancies suggest that the calibration

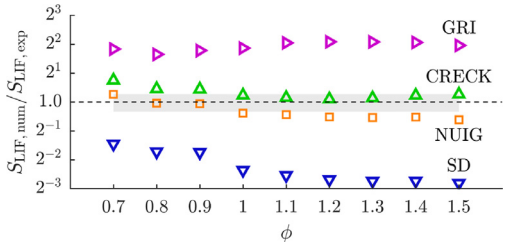

Fig. 4. Numerical $S_{\mathrm{LIF,num}}$ normalized by the experimental signal intensity at $z = 2.5$ mm. The dashed line indicates a perfect agreement between experiments and simulations and the grey band represents the total experimental uncertainty.

of major formation pathways only (thermal and prompt) would result in incorrect "optimal" reaction rates for the secondary routes. The effect of such modeling errors become more prominent as exotic fuel blends and premixed, lean combustors are increasingly used to reduce emissions, leading to almost evenly distributed contributions of each production route. Recent hierarchical mechanisms used in this work provide a significantly better agreement with measured profiles. The NUIG mechanism slightly over-predicts NO formation in lean flames, but under-predicts in richer flames. Profiles obtained with the CRECK mechanism exhibit good agreement with rich flames, but the discrepancy with measurements increases in leaner conditions, where a complex interaction between formation routes is suspected.

The impact of the nitrogen chemistry is isolated in Fig. 3(j–l) by using the same base chemistry of the NUIG mechanism, which showed the best agreement with reactivity measurements, and taking the nitrogen chemistry from the different models studied. The discrepancy is amplified for the modified GRI and CRECK models with an increased production of NO in the flame front. These results suggest that the tuning of reaction rate constants can generate nominal mechanisms that agree well with validation targets, but for the wrong reasons. It further highlights the need for independent experiments designed to target a minimal set of reactions. The current data set in low-temperature hydrogen flames provides relevant measurements for optimization and validation of thermochemical mechanisms, and especially the nitrogen submechanism, by focusing on small chemical subsets at a time.

To ease comparison between all cases studied, Fig. 4 presents the nominal numerical LIF signal intensity normalized by the experimental measurements at an axial location of 2.5 mm upstream of the stagnation surface. The comparison is performed sufficiently downstream of the flame to have fully developed NO profiles, while being outside the thermal boundary layer close to the

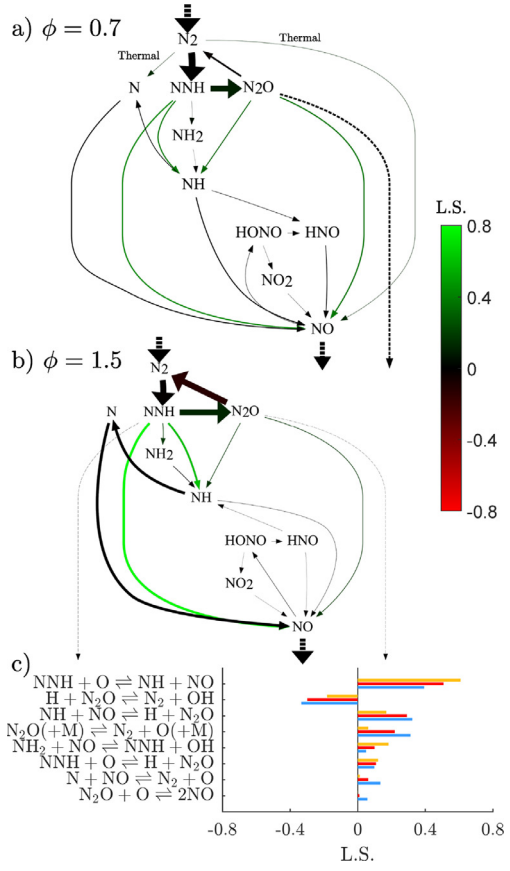

Fig. 5. RPA shown for (a) $\phi = 0.7$ and (b) $\phi = 1.5$. Arrows are scaled by the flux of N-atoms where only fluxes $> 1\%$ are shown for clarity. Dashed arrows represent fluxes entering and leaving the control volume. The red-to-green coloring is obtained from sensitivity analyses. The sensitivity to individual reactions in the nitrogen chemistry is shown in (c) for $\phi = [0.7, 1.0, 1.5]$ by blue, red, and yellow bars, respectively.

cooled plate. A unity ratio indicates perfect agreement between simulations and experimental data. The uncertainty expressed by the shaded gray area includes experimental uncertainties presented in Fig. 3 and an estimated error obtained from the propagation of boundary condition uncertainties in the simulations [2]. The uncertainty from boundary conditions is obtained from

$$\sigma_{S_{\mathrm{LIF,num}}/S_{\mathrm{LIF,exp}},\mathrm{BC}} = \sqrt{\Sigma[\mathrm{L.S.}(x_i) \cdot \sigma_{x_i}]^2}\,, \qquad (4)$$

where the logarithmic sensitivity (L.S.) of the signal ratio to a change in parameter x_i multiplies its measured uncertainty σ_{x_i}. The total uncertainty in the signal ratios evaluated with Eq. (5) becomes an estimate of all uncertainty sources, except from modeling errors in mechanisms and LIF models. Predictions outside this area indicate modeling

inaccuracies, making the present data set valuable for calibration of the nitrogen chemistry.

$$\sigma_{S_{\mathrm{LIF,num}}/S_{\mathrm{LIF,exp}}=1} = \sqrt{\sigma^2_{S_{\mathrm{LIF,num}}/S_{\mathrm{LIF,exp}},\mathrm{BC}} + \sigma^2_{S_{\mathrm{LIF,exp}}}} \tag{5}$$

As observed previously, predictions from the GRI and SD mechanisms lie significantly outside the uncertainty band and the best agreement is found with the NUIG and CRECK mechanism for lean and rich cases, respectively. Both mechanisms exhibit a similar decreasing LIF signal intensity ratio which stabilizes and remains relatively constant in rich flames.

The NO production routes are identified with Reaction Pathway Analyses [2] by tracking the flux of reacting atomic nitrogen (a conserved scalar) as reactants are transformed into products. Network graphs are generated to visualize chemical interactions and quantify the fraction of atoms entering each NO formation pathway. Results are shown in Fig. 5(a) and (b) for the lean and rich cases, respectively, where arrow widths are scaled by the fluxes between species and only fluxes larger than 1% are displayed. They are produced with the NUIG mechanism with the outlet of the control volume located 2.5 mm from the stagnation plate, corresponding to the cases presented in Fig. 4. Red-to-green coloring is obtained from the L.S. of NO concentration at the desired axial location to sequential changes in specific reaction rates by 1% through brute-force sensitivity analysis. The L.S. value is evaluated as the sum of the sensitivity of all reactions involving the two species.

In the lean flame (Fig. 5a), NO is formed mostly via the NNH route with a small contribution through the thermal pathway which explains the rise in signal intensities observed in the post-flame region for this lean flame (Fig. 3). As equivalence ratio is increased to $\phi = 1.5$ (Fig. 5b), slightly lower flame temperatures and lack of excess oxygen prevent the formation of nitric oxide through the thermal pathway. At atmospheric pressure and under low flame temperature, N_2O recycles to N_2 suggesting that the N_2O route does not contribute to emissions and that the production of NO is solely a function of the NNH route in the current measurements.

The sensitivity analysis shows that few paths in the RPA affect the formation of nitric oxide, although individual reactions might have strong effects as shown in Fig. 5(c) for important reactions. Direct conversions from NNH and N_2O to nitric oxide are favoured, as expected, but other paths in the nitrogen chemistry remain mostly unaffected by changes in specific reaction rates. This is the case for the N_2 to N_2O path as the initiation reaction $N_2O(+M) \leftrightharpoons N_2 + O(+M)$ with positive L.S. competes with recycling reactions with negative L.S. where N_2O reacts with H or O radicals back to N_2. The lack of sensitivity to the initiation reaction $NNH \leftrightharpoons N_2 + H$ indicates that NNH is in quasi-steady state as defined in the nitrogen chemistry [3,28]. The production of NO through the NNH route becomes proportional to the equilibrium constant of the initiation reaction and the specific rate constant of the reaction $NNH + O \leftrightharpoons NH + NO$.

4. Conclusion

This paper presents velocity, temperature, and NO concentration measurements performed in premixed, jet-wall stagnation, hydrogen–air flames at atmospheric pressure, diluted with argon to maintain flame temperatures near 1800 K. One-dimensional profiles are measured using particle tracking velocimetry and laser-induced fluorescence for equivalence ratios from 0.7–1.5. Sufficiently low flame temperatures minimize the formation of nitric oxide through the thermal pathway, even suppressing it in rich conditions due to the lack of excess oxygen. Resulting experimental profiles are therefore dominated by the NNH and N_2O pathways.

Comparison with five mechanisms from the literature shows significant discrepancies between measurements and predictions, indicating that the foundation for combustion chemistry still requires further refinement. A recently updated mechanism from NUIG provides the best overall agreement with reference flame speed measurements across the range of equivalence ratios while other mechanisms under-predict the reactivity of the mixture. The NO formation is over- and under-predicted by the "small" detailed mechanisms for hydrocarbon combustion, GRI-Mech 3.0 and San Diego v2016, but captured within experimental uncertainties for the hierarchical NUIG and CRECK models. However, comparison of the NO profiles obtained using a common H_2/O_2 chemistry and different nitrogen models shows that discrepancies in the base chemistry can lead to good agreement with experiments but for different reasons.

Reaction pathway analyses performed with the NUIG mechanism identify NNH as the dominant NO production route for the low-temperature, atmospheric-pressure cases presented. N_2O recycles to N_2 preventing the overall formation of nitric oxide through the pressure-dependent route. It highlights the importance of not only understanding the NNH route but also its interactions with the N_2O mechanism. Setting NNH in quasi-steady state in the nitrogen chemistry leads to relatively good agreement with experimental data, suggesting this is an adequate description of the physics.

The designed experiments provide an accurate experimental data set that isolates minor formation pathways. Accurate boundary conditions allow the

measurements to be used as validation and calibration targets for the development of thermochemical mechanisms.

Declaration of Competing Interest

None.

Acknowledgments

The authors wish to acknowledge the support of the Fonds de recherche Nature et Technologies du Québec, Natural Sciences and Engineering Research Council of Canada (NSERC), and Siemens Canada Limited.

Supplementary material

Supplementary material associated with this article can be found, in the online version, at doi:10.1016/j.proci.2020.06.124.

References

[1] T. Lieuwen, M. Chang, A. Amato, *Combust. Flame* 160 (8) (2013) 1311–1314, doi:10.1016/j.combustflame.2013.05.001.
[2] P. Versailles, A. Durocher, G. Bourque, J.M. Bergthorson, *Proc. Combust. Inst.* 37 (1) (2019) 711–718.
[3] P. Glarborg, J.A. Miller, B. Ruscic, S.J. Klippenstein, *Prog. Energy Combust. Sci.* 67 (2018) 31–68.
[4] R. Sausa, W. Anderson, D. Dayton, C. Faust, S. Howard, *Combust. Flame* 94 (4) (1993) 407–425.
[5] J.E. Harrington, G.P. Smith, P.A. Berg, A.R. Noble, J.B. Jeffries, D.R. Crosley, *Proc. Combust. Inst.* 26 (2) (1996) 2133–2138.
[6] G.J. Rørtveit, J.E. Hustad, S.-C. Li, F.A. Williams, *Combust. Flame* 130 (1–2) (2002) 48–61.
[7] M. Skottene, K.E. Rian, *Int. J. Hydrog. Energy* 32 (15) (2007) 3572–3585.
[8] Z. Hong, D.F. Davidson, R.K. Hanson, *Combust. Flame* 158 (4) (2011) 633–644.
[9] A. Durocher, P. Versailles, G. Bourque, J.M. Bergthorson, *Combust. Sci. Technol.* (2019) 1–27.
[10] H. Wang, D.A. Sheen, *Prog. Energy Combust. Sci.* 47 (2015) 1–31.
[11] P. Versailles, A. Durocher, G. Bourque, J.M. Bergthorson, *J. Eng. Gas Turbine Power* 141 (1) (2019) 011027.
[12] D. Goodwin, H. Moffat, R. Speth, Cantera: An Object-Oriented Software Toolkit for Chemical Kinetics, Thermodynamics, and Transport Processes, 2016 doi:10.5281/zenodo.170284.
[13] F. Yang, C.K. Law, C. Sung, H. Zhang, *Combust. Flame* 157 (1) (2010) 192–200.
[14] J. Bergthorson, P. Dimotakis, *Exp. Fluids* 41 (2) (2006) 255–263.
[15] P. Versailles, A. Durocher, G. Bourque, J.M. Bergthorson, *ASME Turbo Expo 2019*, ASME Digital Collection, 2019.
[16] G.M.G. Watson, P. Versailles, J.M. Bergthorson, *Combust. Flame* 169 (2016) 242–260, doi:10.1016/j.combustflame.2016.04.015.
[17] P. Paul, J. Gray, J. Durant, J. Thoman, *AIAA J.* 32 (8) (1994) 1670–1675.
[18] M. Tamura, P.A. Berg, J.E. Harrington, J. Luque, J.B. Jeffries, G.P. Smith, D.R. Crosley, *Combust. Flame* 114 (3–4) (1998) 502–514.
[19] G.M.G. Watson, P. Versailles, J.M. Bergthorson, *Proc. Combust. Inst* 36 (1) (2017) 627–635, doi:10.1016/j.proci.2016.06.108.
[20] B. Connelly, B. Bennett, M. Smooke, M. Long, *Proc. Combust. Inst.* 32 (1) (2009) 879–886.
[21] J. Luque, D. Crosley, LIFBASE Database and Spectral Simulation Program (Version 2.1.1), *Technical Report*, SRI International, 2013.
[22] T. Lee, W.G. Bessler, H. Kronemayer, C. Schulz, J.B. Jeffries, *Appl. Opt.* 44 (31) (2005) 6718–6728.
[23] G.P. Smith, D.M. Golden, M. Frenklach, N.W. Moriarty, B. Eiteneer, M. Goldenberg, C.T. Bowman, R.K. Hanson, S. Song, W.C.J. Gardiner, V.V. Lissianski, Z. Qin, GRI-Mech 3.0, 1999.
[24] University of California at San Diego, Chemical-Kinetic Mechanisms for Combustion Applications, 2016.
[25] E. Ranzi, A. Frassoldati, R. Grana, A. Cuoci, T. Faravelli, A. Kelley, C.K. Law, *Prog. Energy Combust. Sci.* 38 (4) (2012) 468–501.
[26] C.-W. Zhou, Y. Li, U. Burke, C. Banyon, K.P. Somers, S. Ding, S. Khan, J.W. Hargis, T. Sikes, O. Mathieu, et al., *Combust. Flame* 197 (2018) 423–438.
[27] A.A. Konnov, *Combust. Flame* 203 (2019) 14–22.
[28] S.J. Klippenstein, L.B. Harding, P. Glarborg, J.A. Miller, *Combust. Flame* 158 (4) (2011) 774–789.